J. Fluid Mech. (2008), *vol.* 609, *pp.* 349–375.
doi:10.1017/S0022112008002425 Printed in the United Kingdom

Mixing of two thermal fields emitted from line sources in turbulent channel flow

E. COSTA-PATRY AND L. MYDLARSKI

Department of Mechanical Engineering, McGill University, 817 Sherbrooke Street West, Montréal, QC, H3A-2K6, Canada

(Received 23 August 2007 and in revised form 12 May 2008)

The interaction of two passive scalars (both temperature in air) emitted from concentrated line sources in fully developed high-aspect-ratio turbulent channel flow is studied. The thermal fields are measured using cold-wire thermometry in a flow with a Reynolds number (Uh/ν) of 10 200.

The transverse total root-mean-square (RMS) temperature profiles are a function of the separation distance between the line sources (d/h), their average wall-normal position ($y_{s_{av}}/h$), and the downstream location (x/h), measured relative to the line sources. Similarly, profiles of the non-dimensional form of the scalar covariance, the correlation coefficient (ρ), are a function of the same parameters and quantify the mixing of the two scalars.

The transverse profiles of the correlation coefficient are generally largest at the edges of the thermal plume and smallest in its core. When the line sources are not symmetrically located about the channel centreline, the minimum in the correlation coefficient transverse profiles drifts towards the (closer) channel wall. For source locations that are equidistant from the channel centreline, the minimum correlation coefficient occurs at the centreline, due to the underlying symmetry of this geometry. The initial downstream evolution of the correlation coefficient depends significantly on d/h, similar to that in homogeneous turbulence. However, there is always a dependence on $y_{s_{av}}/h$, which increases in importance as both the downstream distance is increased and the wall is approached. Lastly, the correlation coefficient profiles tend towards positive values in the limit of large downstream distances (relative to the source separation), though further measurements farther downstream are required to confirm the exact value(s) of their asymptotic limit(s).

Spectral analysis of the cospectra and coherency spectra indicates that the large scales evolve more rapidly than the small ones. Furthermore, the fast evolution of the large scales was most evident when the sources were located close to the wall. This presumably derives from the large-scale nature of turbulence production, which is strong in the near-wall region.

1. Introduction

The mixing of a scalar (e.g. energy, mass, etc.) within turbulent flows is a phenomenon of relevance to a broad range of processes, including meteorology, oceanic science, heat transfer, combustion, and environmental pollutant dispersion. To accurately predict and model such processes, a thorough understanding of turbulent scalar mixing is required. Reviews of the subject have been compiled by Sreenivasan (1991), Shraiman & Siggia (2000) and Warhaft (2000).

Recent research has shown that the complexity of turbulent scalar mixing originates from the mixing process itself, rather than being inherited from the intrinsically nonlinear and complex velocity field (Kraichnan, 1968, 1974, 1994; Shraiman & Siggia 2000). One of the complications inherent to the scalar mixing process derives from the manner in which the scalar is injected into the turbulent flow – the scalar can be introduced into the flow at scales that are different from that of the velocity field. As a result, this 'injection scale' can dominate the evolution of the passive scalar field – see, for example, Warhaft & Lumley (1978), Sreenivasan *et al.* (1980), Durbin (1982), Villermaux, Innocenti & Duplat (2001), or Beaulac & Mydlarski (2004).

A fundamental problem in the study of turbulent scalar mixing is posed when the scalar is introduced into the flow at a scale that is smaller than the smallest scales of the velocity field (e.g. Taylor 1935). An extension of this problem – with applications to combustors, chemical reactors, heat exchangers, and environmental dispersion of multiple scalars – is the interaction of scalar fields emitted from two (or more) concentrated sources. In this case, the scalar mixing will be a function of the respective location of the sources, in addition to the properties of the turbulence.

Before proceeding to discuss the objectives of the current research on the mixing of two scalars in turbulent channel flow, we present a review of the literature pertaining to scalar mixing from one or more concentrated sources in turbulent flows.

The dispersion of a scalar from a single source in turbulent flows has been extensively discussed in the literature. In most cases, temperature was the injected scalar. A detailed review of the literature on this subject can be found in Lavertu & Mydlarski (2005), which is summarized here.

Dispersion from a thermal line source in grid turbulence was the first problem of this nature to be studied. Scalar dispersion experiments in grid turbulence were performed by Taylor (1935), Uberoi & Corrsin (1953), and Townsend (1954), who published results on the evolution of the mean and fluctuating temperature fields. Subsequent research showed that the mean temperature profiles downstream of a thermal line source in homogeneous isotropic turbulence were Gaussian and that their evolution could be be divided into three stages: (i) the molecular diffusive range, for which $t \ll (\kappa/\langle v^2 \rangle)$, where t is time, κ is the thermal diffusivity and v is the transverse velocity fluctuation; (ii) the turbulent convective range, $(\kappa/\langle v^2 \rangle) \ll t \ll t_L$, where t_L is the Lagrangian time scale; and (iii) the turbulent diffusive range where $t \gg t_L$ (Warhaft 1984; Anand & Pope 1985; Stapountzis *et al.* 1986). The root-mean-square (RMS) temperature (θ_{rms}) profiles were found to be initially double-peaked, a phenomenon that disappears and then reappears when the thermal plume is much larger than the integral scale.

Karnik & Tavoularis (1989) measured the diffusion of heat from a line source in a homogeneous uniformly sheared turbulent flow. They found that the mean scalar profile slowly drifted from behind the source location towards the lower-velocity region. The appearance, disappearance and re-appearance of double peaks in the transverse profiles of θ_{rms} were also observed.

Inhomogeneous shear flows are usually divided into two families: wall-bounded shear flows and free shear flows. The first includes boundary layer flows and internal flows. The latter includes wakes, jets and mixing layers.

Lavertu & Mydlarski (2005) studied the scalar mixing from a single line source in fully developed turbulent channel flow. They used three line source positions and took measurements at six downstream locations. The source was positioned in a similar manner to the ones used in the present work (parallel to the wall and perdendicular to the flow). Their results include mean profiles, RMS profiles, probability density

functions (PDFs), skewnesses and velocity–temperature correlations. The mean and RMS profiles were well approximated by truncated Gaussian distributions. Important differences between turbulent channel flow, grid-generated turbulence (Warhaft 1984) and homogeneous shear flow (Karnik & Tavoularis 1989) were shown, such as the displacement of the peak RMS temperature towards the centreline in channel flow.

Fundamental work on scalar dispersion in boundary layers was done by Poreh & Cermak (1964) and Poreh & Hsu (1971), who studied the diffusion from a line source in neutrally buoyant conditions. Shlien & Corrsin (1976) studied the mean temperature profiles of a line source placed at different elevations in planar boundary layers. They found that the 'mean temperature profiles approached nearly the same asymptotic shape in all cases'. The dispersion from a line source in both a plane jet and a boundary layer was examined by Paranthoën *et al.* (1988). They developed and applied a rescaling scheme based on the Lagrangian integral time scale of the wall-normal velocity fluctuations at the source location. Their work was successful in collapsing the peak mean temperature onto a single curve. Additional research on the subject was performed by El Kabiri *et al.* (1998), who tested various second-order and third-order closure models on experimental data measured in a boundary layer. Increasing the complexity of the flow, Vinçont *et al.* (2000) studied the dispersion from a line source placed in a boundary layer, downstream of an obstacle. Scalar turbulence in mixing layers was the subject of a study by Veeravalli & Warhaft (1990). It was studied in jets by Incropera *et al.* (1986), Grandmaison, Pollard & Ng (1991) and Tong & Warhaft (1995).

Hanratty and coworkers have made multiple numerical studies of scalar mixing in inhomogeneous flow. His group has studied scalar dispersion in low-Reynolds-number channel flow (Lyons & Hanratty 1991; Papavassiliou & Hanratty 1997; Na & Hanratty 2000). Kontomaris & Hanratty (1994) studied the effects of molecular diffusivity on a point source located at the centreline of a turbulent channel flow and Iliopoulos & Hanratty (1999) simulated the dispersion of fluid particles in inhomogeneous turbulence.

Other computational works include that of Bernard & Rovelstad (1994), who examined the accuracy of a scalar transport model in inhomogeneous turbulence. The turbulent mixing of a passive scalar in pipe flow emitted from a point source was investigated by Brethouwer *et al.* (1999). Orlandi & Leonardi (2004) simulated the behaviour of a passive scalar in turbulent channel flow with wall velocity disturbances in an attempt to emulate rough-wall channels.

Scalar dispersion from multiple concentrated sources – the subject of this work – has received much less attention. The principal work in this field is that of Warhaft (1984), who extended his work on scalar mixing in grid turbulence by studying the interference of two thermal line sources. He determined the correlation coefficient between both scalars (ρ) at eight downstream positions for ten different line source separations (d). His results showed that the evolution of ρ is a function of two parameters: the non-dimensional separation distance d/ℓ, where ℓ is the integral length scale, and the non-dimensional downstream distance $(x'/d)(u/U)$, where x' is the distance from the line source, u the RMS (longitudinal) velocity and U the mean (longitudinal) velocity. He completed his work by experimenting with multiple line sources in an attempt to reinterpret the scalar variance produced by a mandoline.

Tong & Warhaft (1995) investigated the mixing characteristics of temperature fluctuations produced by two fine annular sources placed axisymmetrically at a given downstream position in a turbulent jet. They found that the scalar covariance was strongly dependent on the ring locations and that in 1.5 eddy turnover times the

mixing was complete in all situations. Their coherency spectra increased faster at large scales than at small scales and they found faster rates of mixing in a jet than in grid turbulence.

To aid in modelling competitive-consecutive reactions (reactions where the first is of the form $A + B \rightarrow C$ and a subsequent one is of the form $A + C \rightarrow D$), Vrieling & Nieuwstadt (2003) numerically studied the turbulent dispersion from nearby sources in channel flow. They calculated the scalar covariance resulting from line sources located symmetrically around the channel centreline and compared their results to those of Warhaft (1984) for homogeneous grid turbulence, assuming that the central region of the channel was almost homogeneous.

The objective of the present work is to quantify the interaction of two scalars generated by line sources in fully developed high-aspect-ratio turbulent channel flow. This is undertaken by analysing the scalar covariances and cospectra, while systematically varying the relevant independent variables (e.g. the line source locations). Studying the scalar mixing process in inhomogeneous turbulence will serve to further our understanding of similar phenomena in more realistic flows, such as the atmosphere, internal combustion engines and chemical reactors. Channel flow is selected because it is the simplest realization of an inhomogeneous turbulent flow.

The remainder of the paper is organized as follows. The experimental apparatus is presented in § 2. In § 3, the experimental conditions are evaluated. Results are given in § 4, where (i) scalar field statistical moments, (ii) scalar correlation coefficients, and (iii) scalar cospectra and coherency spectra are described. Conclusions are presented in § 5.

2. Apparatus

The present experiments were carried out in the same open-circuit high-aspect-ratio channel as in Lavertu & Mydlarski (2005). The details of the facility are given in Costa-Patry (2005) and Lavertu & Mydlarski (2005), and will only be summarized herein.

The air flow is provided by a Hudson Buffalo centrifugal blower. It is powered by a 5.6 kW (7.5 hp) AC motor, whose speed is controlled by an ABB ACS 600 frequency converter. Downstream of the blower is a flow-conditioning section consisting of a wide-angle diffuser, a settling chamber (containing an aluminium honeycomb section, followed by six appropriately spaced screens), and a contraction. The flow exiting the contraction (and entering the test section) is uniform and has a low turbulence intensity ($\sim$0.25 %).

The channel test section is 8 m long, 1.1 m high and 0.06 m wide. Its aspect ratio (18) is large enough to ensure that the bottom and top walls do not affect the flow field in the centre of the channel, where all measurements are made. The experiments are performed towards the end of the channel where the flow is fully developed (Lavertu 2002). Probes were inserted through one of two openings in the channel sidewalls. Openings were made in the top and bottom walls of the channel at three different downstream locations to insert the line sources. When an opening is needed for insertion of a probe or a line source, a special port is used. When not required, the openings are plugged so that the walls remain hydrodynamically smooth. The fully developed nature of the flow permits the downstream distance of the probe from the line sources to be varied by moving either the sources or the probe. A linear traversing mechanism, controlled by a precision stepper motor (0.01 mm per step), is used to move probes across the channel.

The line sources are made from fine Nichrome^{TM} wire and are placed vertically in the channel to inject the scalar (temperature). They are kept taut (using weights

Distance (d/h)	Average line source position ($y_{s_{av}}/h$)		
	0.2	0.5	1.0
0.13	A	B	C
0.27	D	E	F
0.50	–	H	I
1.50	–	–	G

TABLE 1. Nomenclature of the nine line sources combinations (A–I). Note the three combinations that are not physically possible.

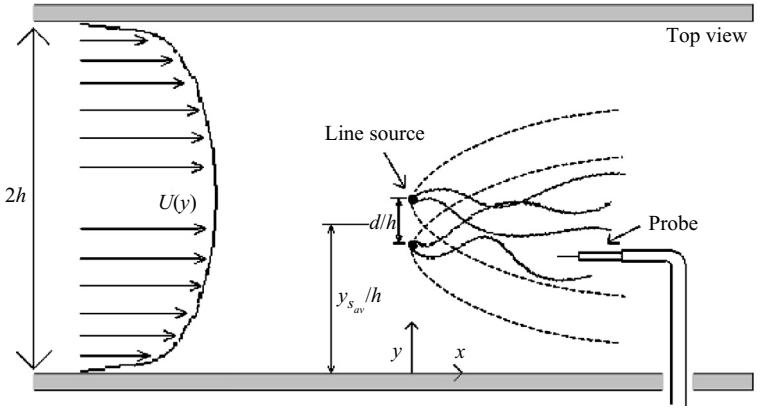

FIGURE 1. Schematic of the experiment. Solid line: instantaneous thermal wake. Dashed line: time-averaged wake.

attached to their ends) to counteract their thermal expansion when heated. Both ends are connected to the terminals of a DC power supply, whose voltage was continuously monitored to ensure that the energy emitted by the line sources was constant. The use of two different line source diameters is required to obtain satisfactory signal-to-noise ratios at large downstream distances. Line sources of 0.127 mm diameter were used for measurements at $x/h = 4.0$ and 7.4. In these cases, the power emitted by each line source was 45 Wm^{-1}. For the other downstream distances, line sources of 0.254 mm diameter were used. The corresponding power was 100 Wm^{-1}. The difference is taken into account in § 4. The measurements made using 100 Wm^{-1} are divided by 2.22 for mean and RMS temperature measurements, and by 2.22^2 for measurements of the temperature variance and spectra, for comparison with measurements made using 45 Wm^{-1}.

The source locations can be specified in terms of the wall-normal distance of each source (y_{s_1} and y_{s_2}). However, in addition to facilitating a comparison with homogeneous flows (where the line source separation is the relevant quantity), it is more logical to specify the source locations in terms of their average wall-normal distance, $y_{s_{av}} (= (y_{s_1} + y_{s_2})/2$, which is directly related to the inhomogeneity of the flow) and the distance between the two lines sources, d $(= y_{s_1} - y_{s_2})$. See figure 1.

In total, 54 different cases are studied. Six downstream distances are used: $x/h = 4.0$, 7.4, 10.8, 15.2, 18.6 and 22.0. Nine combinations of wall-normal source locations were chosen. These combinations cover the regions of interest in the channel. Table 1

presents the line source positions that are used herein and specifies the nomenclature used to describe them.

Though the principal results of the present work pertain to the measurement of temperature, hot-wire anemometry was employed to measure the (longitudinal) velocity field to characterize the flow (see § 3). Tungsten hot wires of 3.05 μm diameter were operated at an overheat of 1.8 using a TSI IFA 300 constant-temperature hot-wire anemometer. The length-to-diameter ratio of the hot wires was approximately 200. TSI 1210 (single-normal) or TSI 1218 (boundary-layer) probes were used. The hot-wires were calibrated using a TSI 1127 calibration jet with a precision MKS 220D pressure transducer.

Cold-wire thermometry was used to measure the temperature field. The cold wires were made of Wollaston wire (with a 0.63 μm diameter platinum core) and soldered to TSI 1210 single-wire probes. The former were operated by a cold-wire thermometer built at the Université Laval (Québec, Canada) and based on the constant-current anemometry circuit given by Lemay & Jean (2001) and Lemay & Benaïssa (2001). The cold wires were calibrated in the same facility as the hot wires, which was modified to incorporate electric heating of the air upstream of the calibration jet inlet. The length of the cold wires was approximately 0.5 mm (i.e. $l_{wire}/d_{wire} \approx 800$) and the probe current was 100 μA. The former choice was a compromise between the competing effects of (i) spatial resolution and (ii) conduction between the cold wire and its prongs (Browne & Antonia 1987). See Mydlarski & Warhaft (1998) for more details on this subject. LaRue, Deaton & Gibson (1975) showed that the −3 dB point of the frequency response of a 0.63 μm diameter platinum cold wire is ∼5 kHz (when the flow velocity is 5 m s^{-1}). The Kolmogorov frequencies ($f_\eta \equiv \langle U \rangle/(2\pi\eta)$) herein are approximately 3 kHz. Thus, the cold-wire thermometer has sufficient temporal resolution that a compensation scheme (such as that of Lemay & Benaïssa 2001) was not necessary.

The output voltages of the hot-wire anemometer and the cold-wire thermometer were both high- and low-pass filtered using a Krohn-Hite 3382 band-pass filter. The high-pass filter frequency was set to 0.1 Hz to eliminate any low frequency non-turbulent fluctuations. The low-pass filter frequency was set slightly above the Kolmogorov frequency (for the given measurement location) to eliminate any high-frequency noise. The voltages were then digitized using a 16-bit analog-to-digital board (National Instruments PCI-6036E), controlled by LabVIEW. Statistical moments of fluctuating quantities were recorded using data sets consisting of 4.096×10^4 samples recorded at 200 Hz (for a corresponding record duration of 3.4 min). This sampling frequency corresponds to roughly the inverse of the integral time scale of the measured quantities. Spectral data sets (for the calculation of scalar cospectra) consisted of 4.096×10^5 data points. These were sampled at twice the low-pass filtering frequency. Convergence of these quantities was confirmed in Costa-Patry (2005).

It should be mentioned that the scalar covariances (and cospectra) are calculated herein from measurements of the scalar field itself using the method of inference (Warhaft 1981), which employs a sequence of three measurements in which (i) one line source, (ii) the other line source, and (iii) both line sources are energized. The scalar covariance arises in the expression of the total variance, defined as

$$\langle \theta_{1+2}^2 \rangle = \langle (\theta_1 + \theta_2)^2 \rangle = \langle \theta_1^2 \rangle + \langle \theta_2^2 \rangle + 2\langle \theta_1 \theta_2 \rangle.$$

Using this relationship, the scalar covariance can be estimated from the above-mentioned three quantites:

$$\langle \theta_1 \theta_2 \rangle = \tfrac{1}{2}\big(\langle (\theta_1 + \theta_2)^2 \rangle - \langle \theta_1^2 \rangle - \langle \theta_2^2 \rangle\big),$$

$\langle U\rangle_{y/h=1}$ [m s^{-1}]	5.2
$u_{rms_{y/h=1}}$ [m s^{-1}]	0.19
$u_\star$ [m s^{-1}]	0.26
$\epsilon_{y/h=1}$ [m^2 s^{-3}]	0.57
$\eta_{y/h=1}(\equiv(\nu^3/\epsilon)^{3/4})$ [mm]	0.28
$Re(=\langle U\rangle_{y/h=1}h/\nu)$	10200
$Re_\tau(=u_*h/\nu)$	510

TABLE 2. Flow parameters. $h=0.030\,\mathrm{m}$; $\nu=15.3\times10^{-6}$ m^2 s^{-1}.

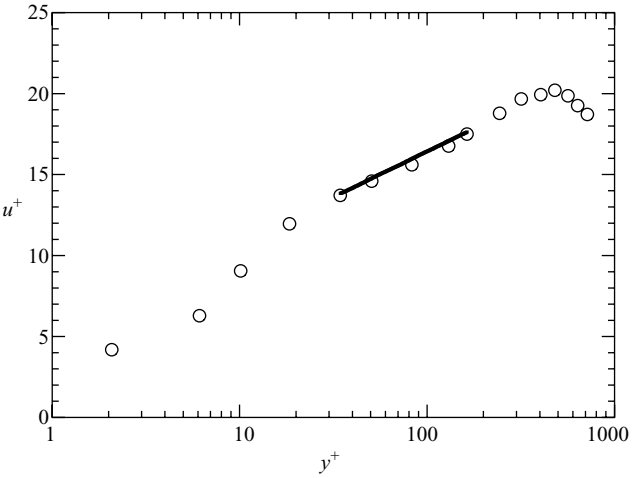

FIGURE 2. Mean velocity profile plotted in wall units. The solid line corresponds to the log-law.

where all three terms on the right-hand side are independently measured. Cospectra can be calculated from an analogous relationship between the three measured scalar spectra.

3. Experimental conditions and sources of error

The details of the experimental conditions and sources of error are summarized in this section. For more information, see Costa-Patry (2005).

The flow consisted of fully developed high-aspect-ratio turbulent channel flow. The agreement between the measured velocity profile and the log-law was within 2 %.† The properties of the flow are specified in table 2. The velocity profile is shown in figure 2.

The temperature–velocity correlations emanating from a single line source were measured by Lavertu (2002), who showed that the ratio of buoyant production to dissipation is at most 1.7 %. Thus the scalar can be considered to be passive. Furthermore, Lavertu (2002) showed that the thermal fields produced by 0.127 mm and 0.254 mm diameter line sources were statistically identical and therefore independent

† The quoted error applies for $y^+>30$ and $y/h<0.3$ – the range of applicability of the log-law (Pope 2000), defined by $u^+=(1/\kappa)\ln(y^+)+B$, where $u^+\equiv\langle U\rangle/u_\star$, $y^+\equiv u_\star y/\nu$, $u_\star\equiv\sqrt{\nu(\mathrm{d}\langle U\rangle/\mathrm{d}y)_{y=0}}$, $\kappa=0.41$ and $B=5.2$.

of source diameter. Lastly, the channels walls can be approximated as being adiabatic, as detailed in Lavertu (2002).

Costa-Patry (2005) performed a series of tests to verify the symmetry of the scalar field about the channel centreline. These included: (i) measuring the probability density functions (PDFs) of the scalar field emitted from a centreline source at transverse locations equidistant from the centreline, and (ii) confirming the even symmetry (about the channel centreline) of the RMS scalar profile generated by a pair of line sources symmetrically located about the channel centreline (e.g. $y_{s_{av}}/h = 1.0$ and $d/h = 1.50$). All tests confirmed the necessary symmetries of the scalar field.

There are two sources of wall-normal positioning error. First, the wall-to-line-source distance has a maximum positioning error of ± 0.15 mm. Secondly, the error in estimating the wall-to-probe distance is ± 0.20 mm. Thus the total positioning error in the wall-normal direction is ± 0.35 mm or ± 1.2 % of h. Downstream distances are accurate to within 1 mm ($x/h = 0.033$).

Background thermal noise with contributions between the high- and low-pass filtering frequencies is not removed by the previously mentioned band-pass filters. However, it was measured before and after each experiment and subtracted from all measurements (on a mean-square basis, assuming zero correlation between the signal and the noise). Note that experiments were only performed when the background RMS thermal noise was less than 0.06°C.

4. Results

The results are divided into a discussion of the scalar field statistical moments (§ 4.1), the scalar correlation coefficients (§ 4.2) and the scalar cospectra and coherency spectra (§ 4.3). As expected, the cospectra and coherency spectra for the 54 cases represent a large amount of data. Therefore, only selected results containing the important elements will be presented in this last subsection.

4.1. *Scalar field statistical moments*

Mean temperature profiles for a single line source in turbulent channel flow were thoroughly discussed in Lavertu & Mydlarski (2005). They found that the transverse peak location of the mean profile stays at the line source position, y_s/h, for the range of x/h studied. The mean profiles were reasonably well approximated by truncated Gaussian distributions, though their accuracy decreased with increasing downstream distance. The mean peak temperature excesses were found to decay as $x^{-0.7}$.

Given that the advection–diffusion equation is linear in temperature (when considering passive scalars), the mean temperature profiles behind two line sources can be deduced from the superposition of those produced by a single source. This is verified in figure 3. Consequently, mean temperature profiles formed by multiple line sources can be inferred from the results of Lavertu & Mydlarski (2005) and are not discussed herein.

Figure 4 presents the transverse normalized θ_{rms} profiles for the nine combinations of line source locations. The θ_{rms} profiles depend on d/h, $y_{s_{av}}/h$ and x/h. If the plumes are barely interacting (which corresponds to large d/h and/or small x/h), then the θ_{rms} profiles are well separated and double peaks dominate. Double peaks in the θ_{rms} profiles emitted from two scalar sources were also observed in grid turbulence by Warhaft (1984) and in numerical simulations of turbulent channel flow by Vrieling & Nieuwstadt (2003).

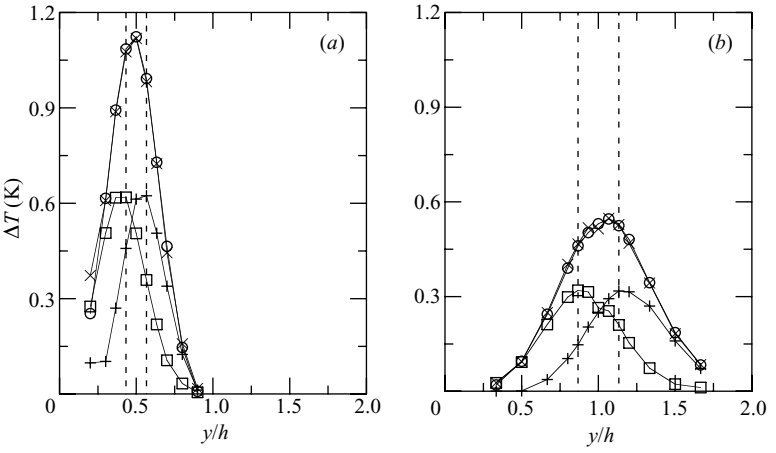

FIGURE 3. Typical transverse mean temperature excess ($T - T_\infty$) profiles. (*a*) Case B, $x/h = 4.0$. (*b*) Case F, $x/h = 10.8$. The vertical dashed lines are drawn at the locations of the line sources. ○: Both line sources energized. □: Left line source energized. +: Right line source energized. ×: Algebraic sum of □ and +.

When $y_{s_{av}}/h = 0.2$, double peaks were not witnessed, though they presumably occur for $x/h < 4$, before the merging of the two thermal wakes. This accelerated blending of two near-wall thermal wakes into one can be linked to the presence of (i) the boundary, which concentrates the heat on one side of the line source, and (ii) the higher turbulent kinetic energy in this zone. For source locations with $y_{s_{av}}/h = 1.0$, double peaks are present for a much longer time and for all d/h. The larger d/h cases are slower in merging their thermal wakes and the double peaks remain. For example, some thermal wakes are clearly not interacting (e.g. case G). Profiles with $y_{s_{av}}/h = 0.5$ present hybrid characteristics; they start as double peaked and become single peaked at larger x/h. The θ_{rms} profiles measured in homogeneous turbulence by Warhaft (1984) most closely resemble those of the present work when $y_{s_{av}}/h = 1.0$. This is expected given that the centre of the channel is the least inhomogeneous part of the flow.

It is also worth noting that the peaks of the θ_{rms} profiles for combinations with $y_{s_{av}}/h = 0.2$ and 0.5 move towards the channel centreline. A similar peak movement was also observed for plumes emitted from single line sources (Lavertu & Mydlarski 2005). Therein, it was shown that the displacement rate of the peaks is a function of the line source location: the closer to the wall, the faster the displacement. The same observation holds in the present case; the movement of the peak accelerates as the average line source location moves away from the channel centreline, towards the wall.

It has been observed that the peak of the θ_{rms} profiles ($\theta_{rms\text{–}peak}$) generated by a single line source in different turbulent flows follows a power-law decay in x: $\theta_{rms\text{–}peak} \propto x^n$. Figure 5 presents the downstream evolution of $\theta_{rms\text{–}peak}$ for the nine combinations. It was found that the decay is proportional to $n = -0.9$ when only one line source is energized, consistent with the results of Lavertu & Mydlarski (2005) for a single line source in channel flow. In homogeneous turbulent shear flow, Karnik & Tavoularis (1989) found two regimes using a single line source, one having $n = -0.85$ and the other having $n = -1.7$. Warhaft (1984) found, in isotropic turbulence, a value of $n = -0.8$ for $x_o/M \geqslant 3$. In cases where the level of interaction between the thermal

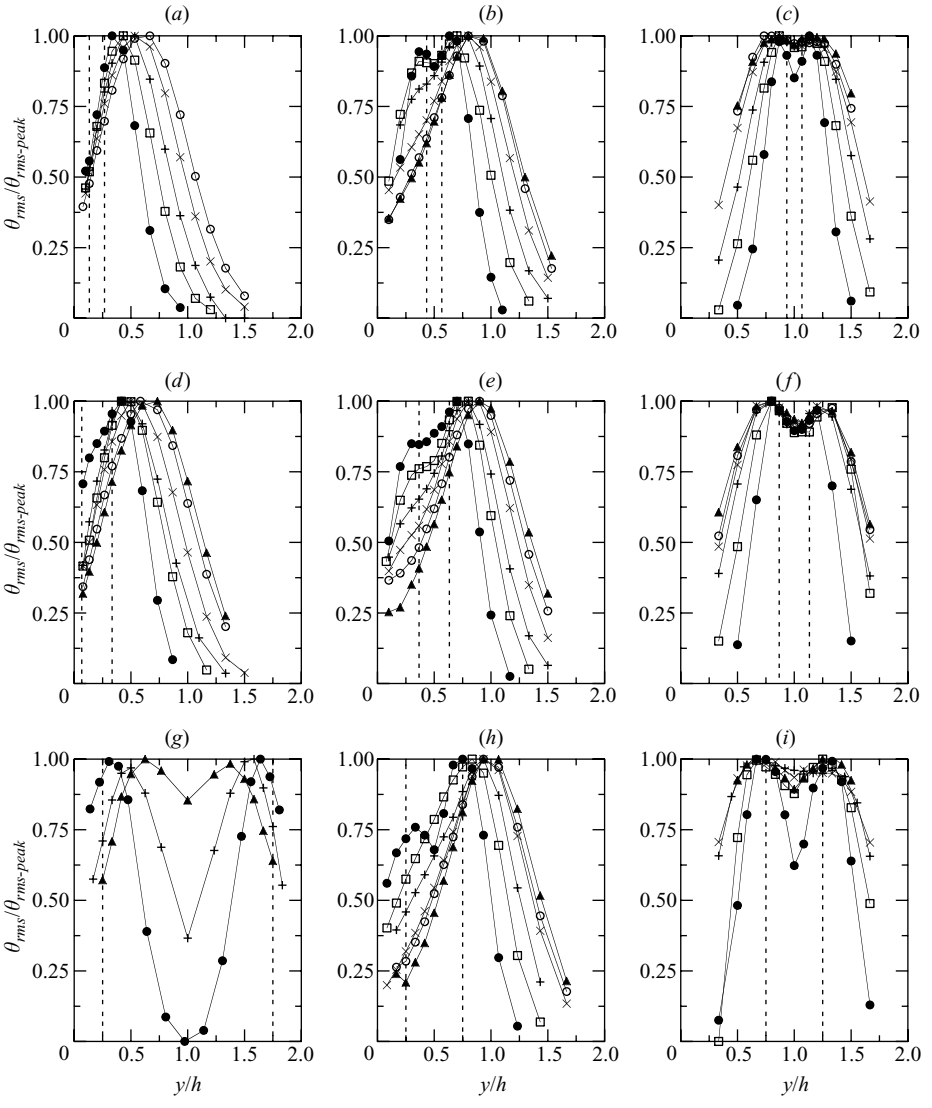

FIGURE 4. Transverse normalized θ_{rms} profiles for the nine combinations of line source locations. (*a*) Case A. (*b*) Case B. (*c*) Case C, etc. The vertical dashed lines are drawn at the locations of the line sources. ●, $x/h = 4.0$; □, $x/h = 7.4$; +, $x/h = 10.8$; ×, $x/h = 15.2$; ○, $x/h = 18.6$; ▲, $x/h = 22.0$.

wakes is negligible, the two-line-source $\theta_{rms\text{–}peak}$ values behave like those behind a single line source and therefore have the same decay exponent. This is true for cases G and I in figure 5. However, when the level of interaction is significant, the decay of the peak of the θ_{rms} profiles for two line sources is less accurately described by a power law, and $\theta_{rms\text{–}peak}$ can be less than, equal to, or greater than the sum of the peak RMS temperatures for the individual line sources.

Figure 6 shows selected θ_{rms} profiles with two line sources energized as well as each line source energized independently. It is clear from figure 6 that the θ_{rms} profile for both line sources energized cannot be directly obtained from the addition of the single-line-source data. The covariance is therefore an important parameter.

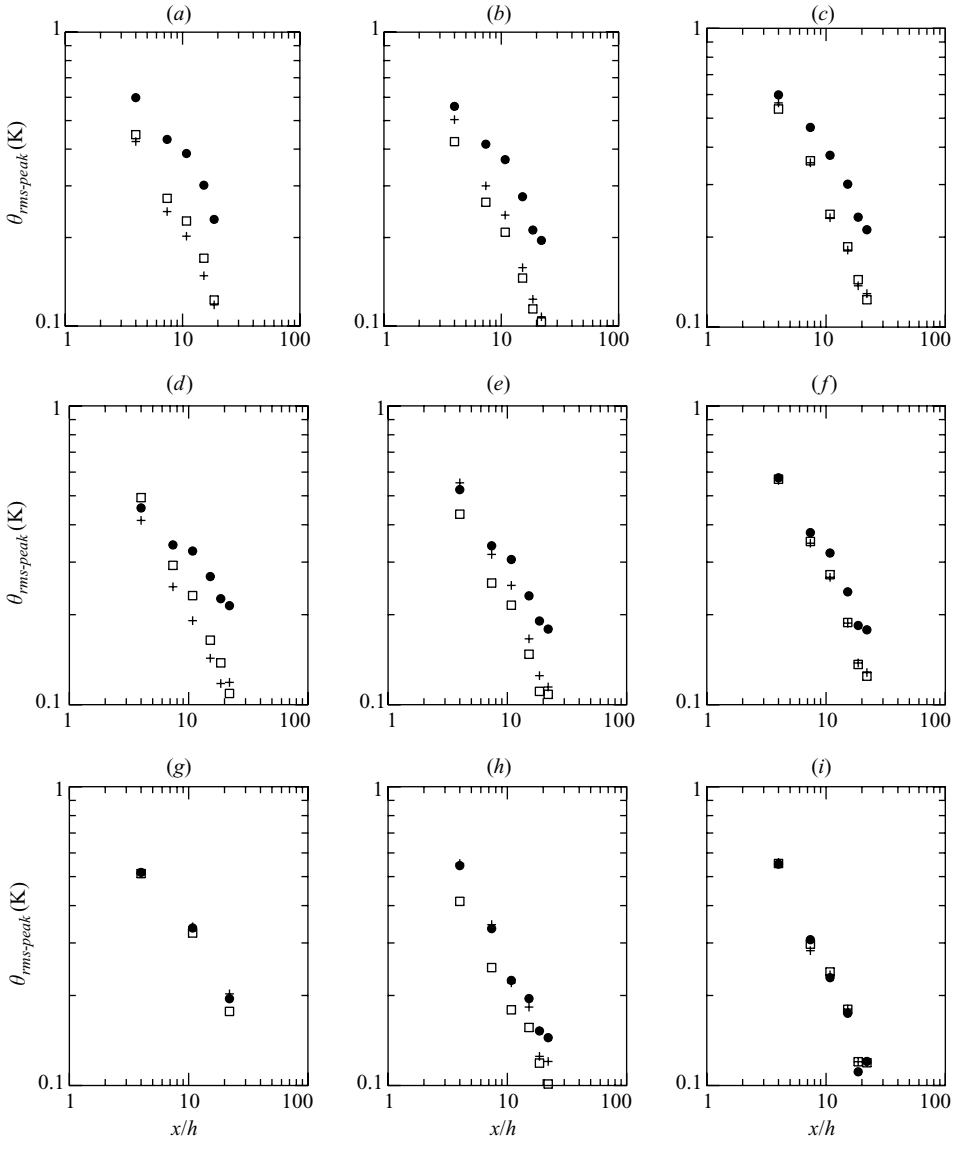

FIGURE 5. Downstream evolution of the peak θ_{rms} for the nine combinations of line source locations. (*a*) Case A. (*b*) Case B. (*c*) Case C, etc. ●, Both line sources energized; □, first line source energized; +, second line source energized.

4.2. *Scalar correlation coefficient evolution*

The non-dimensional form of the scalar covariance ($\langle\theta_1\theta_2\rangle$) is the correlation coefficient:

$$\rho \equiv \frac{\langle\theta_1\theta_2\rangle}{\langle\theta_1^2\rangle^{1/2}\langle\theta_2^2\rangle^{1/2}},$$

which is used to describe the mixing process. The correlation coefficient rates the quality of the mixing process whereas the covariance represents the total amount of mixing. Consequently, ρ can be high in a region where $\langle\theta_1\theta_2\rangle$ is small.

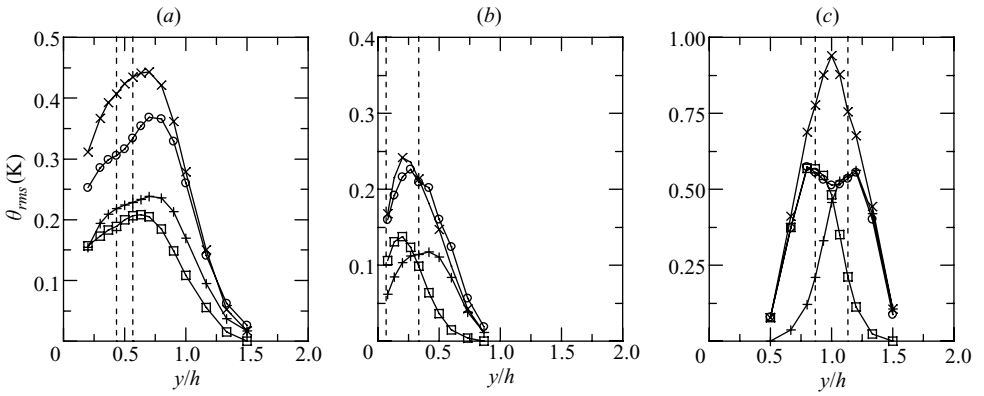

FIGURE 6. Typical transverse θ_{rms} profiles. (*a*) Case B, $x/h = 10.8$. (*b*) Case D, $x/h = 18.6$. (*c*) Case F, $x/h = 4.0$. The vertical dashed lines are drawn at the locations of the line sources. ○, Both line sources energized; □, first line source energized; +, second line source energized; ×, algebraic sum of □ and +.

In turbulent channel flow, ρ is a function of four parameters: the downstream distance (x/h), the wall-normal distance (y/h), the separation between the line sources (d/h) and the average position of the line sources ($y_{s_{av}}/h$). As was the case in § 4.1 for θ_{rms}, all four variables should affect the evolution of the covariance.

Consider the downstream evolution of ρ for transverse locations y such that $y_{s_1} < y < y_{s_2}$. Note that ρ does not exist for small x/h because it is undefined when one (or both) of the scalar variances ($\langle\theta_1^2\rangle$ and/or $\langle\theta_2^2\rangle$) are zero. In other words, ρ is undefined at probe locations that never sample one (or both) of the two plumes. Immediately beyond the region in which ρ is undefined is a region in which, at any time, the probe samples one of the two thermal plumes (or neither of them), but never both simultaneously. In this second region, both plumes are still narrow, and their meandering is dictated by the motions of the largest eddies, which 'flap' them up and down in concert. Here, the probe is rarely exposed to either plume and is predominantly within the free stream between the two plumes. Consequently, the correlation coefficient is effectively zero. As the flapped plumes widen, the probe alternately samples the individual plumes for longer periods (and therefore samples the free stream for shorter ones). As a result, the correlation coefficient becomes increasingly negative, given the anticorrelated fluctuations of the two plumes. The proof that ρ is negative in regions where the plumes never instantaneously overlap was given in Warhaft (1984, p. 375–376). In these regions, the correlation of instantaneous temperature excesses ($\langle\Delta\Theta_1\Delta\Theta_2\rangle$) is zero by definition. ($\Delta\Theta = \Theta - T_\infty = \Delta T + \theta$, where Θ ($= T + \theta$) is the instantaneous temperature and where $\Delta T \equiv T - T_\infty$ is the mean temperature excess, shown in figure 3.) Expansion of $\langle\Delta\Theta_1\Delta\Theta_2\rangle = 0$ indicates that the covariance of the fluctuations $\langle\theta_1\theta_2\rangle$ (and therefore the correlation coefficient) must be negative. When the least amount of time is spent sampling the free stream, the correlation coefficient achieves a minimum before reversing and increasing towards positive values. (Note that the downstream location for which ρ is minimum increases with d/h because the two plumes need to travel farther before they interact for larger d/h.)

The zone in which $\partial\rho/\partial x < 0$ is characterized by the sampling of one wake or the other (but not both). As the plumes broaden and eventually start to mix/overlap, the probe measures in both wakes more and more frequently, and $\partial\rho/\partial x$ becomes positive. In this second zone, the overlapping of the two plumes continually increases,

with a subsequent increase in ρ. When both plumes begin to mix, the correlation of instantaneous temperature excesses ($\langle \Delta\Theta_1 \Delta\Theta_2 \rangle$), which was zero when the plumes did not overlap, becomes positive. (This quantity can never be negative.) As ρ increases from its minimum value to zero, the correlation of instantaneous temperature excesses ($\langle \Delta\Theta_1 \Delta\Theta_2 \rangle$) is smaller than the correlation of mean temperature excesses ($\langle \Delta T_1 \Delta T_2 \rangle$). When ρ is zero, they are both equal. Finally, as ρ tends from zero to its final, maximum value when both plumes are thoroughly mixed, $\langle \Delta\Theta_1 \Delta\Theta_2 \rangle$ exceeds $\langle \Delta T_1 \Delta T_2 \rangle$.

The above-described evolution is controlled by two mechanisms: flapping of the thermal wake and internal turbulent mixing. Both are caused by the turbulence, but are different in their characteristic (length and time) scales. The former is dominant early in the downstream evolution, is caused by the bulk displacement of the thermal wakes, and leads to anticorrelation of the scalar fluctuations. It is a large-scale phenomenon that is dictated by the integral-size eddies. Flapping is present throughout the downstream evolution, but diminishes in relative importance as the thermal wakes widen.

Internal turbulent mixing is effected by eddies of various sizes contained within the thermal plumes. The former mix energy rapidly, and in conjunction with molecular diffusion, bring about mixing at the molecular level, and therefore positive correlation coefficients. (Recall that as long as the two plumes do not overlap, i.e. when $\langle \Delta\Theta_1 \Delta\Theta_2 \rangle = 0$, the covariance $\langle \theta_1 \theta_2 \rangle$ and correlation coefficient must be negative.) As the overlap zone of the plumes broadens with increasing downstream distance, so do the correlation coefficient profiles. The downstream evolution of ρ is the subject of this section.

4.2.1. *Transverse profiles*

The transverse profiles of ρ at different downstream positions for the nine source combinations are shown in figure 7. The correlation coefficient is sensitive to minor changes in the θ_{rms} values. Repetition of the experiments showed that a precision of ± 0.05 in ρ is obtained. If no ρ profile is shown for a given x/h in figure 7, it is because ρ is equal 0 or 1, within experimental error.

We first remark that the maximum values of ρ are found at the edges of the thermal wake. From an instantaneous point of view, the thermal wakes are not continuously present in the tails of the θ_{rms} profiles. Occasionally a large eddy carries part of the plumes there. When the two line sources are close together, a large eddy will move both plumes simultaneously, thus causing the large values of ρ in the tails of the profiles.

The presence of a minimum ρ value close to $y_{s_{av}}/h$ is due to measurements taking place in one wake and then in the other, as discussed above. Early downstream, when the two line sources are close together, integral-size eddies move both thermal wakes simultaneously in the same direction and no instantaneous overlapping of the wakes exists (Warhaft 1984). This leads to a negative correlation coefficient. The minimum in ρ between the sources, as well as the large values of ρ in the tails of the profile, were both observed by Warhaft (1984) and Tong & Warhaft (1995).

The minimum in the transverse profiles of ρ for combinations centred at $y_{s_{av}}/h = 0.2$ and 0.5 moves towards the wall with increasing x/h. Tong & Warhaft (1995) observed a movement of the minimum ρ towards the jet centreline. These phenomena may be related given that, in both cases, the minimum is moving towards a region of high turbulent kinetic energy and, in turbulent channel flow, towards a zone where flapping is less important (due to presence of the wall). Finally, with increasing downstream distance, the internal turbulent mixing increases and the ρ profiles flatten.

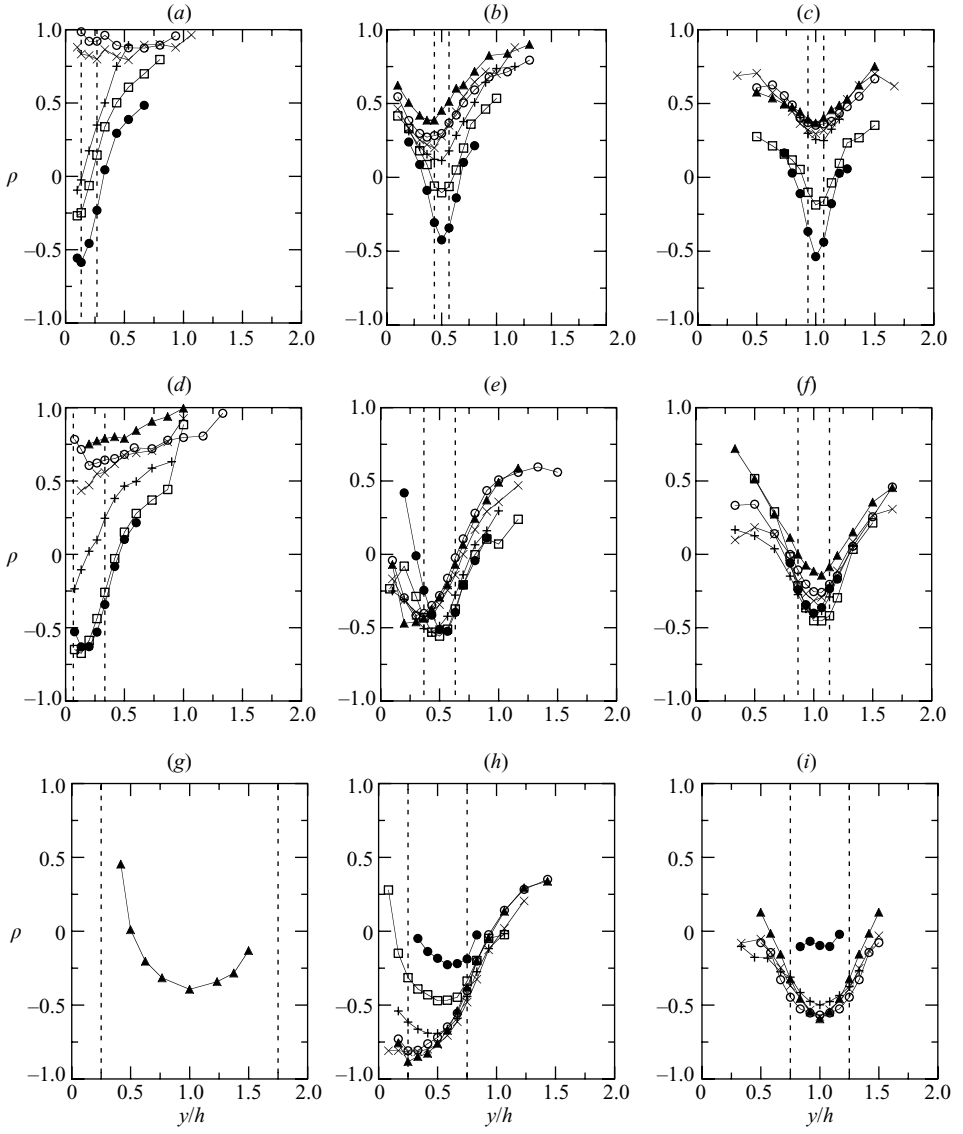

FIGURE 7. Transverse profiles of ρ for the nine combinations of line sources locations. (*a*) Case A. (*b*) Case B. (*c*) Case C, etc. The vertical dashed lines are drawn at the locations of the line sources. ●, $x/h = 4.0$; □, $x/h = 7.4$; +, $x/h = 10.8$; ×, $x/h = 15.2$; ○, $x/h = 18.6$; ▲, $x/h = 22.0$. If no profile is shown for a given x/h, it is because ρ is effectively 0 or 1.

4.2.2. *Evolution of* $\rho_{y_{s_{av}}/h}$

To compare the evolution of different source combinations, both the minimum value of ρ measured in the transverse profile (ρ_{min}) and ρ evaluated at $y = y_{s_{av}}/h$ ($\rho_{y_{s_{av}}/h}$) were studied because they were representative of the profiles of ρ. Warhaft (1984) and Tong & Warhaft (1995) used $\rho_{y_{s_{av}}/h}$ in their analyses. In homogeneous flows, both quantities could be expected to be the same, as is also the case in symmetric, inhomogeneous flows, such as the present one when $y_{s_{av}}/h = 1.0$ (cases C, F, G and I). In these cases, homogeneity and/or symmetry do not require that $\rho_{min} = \rho_{y_{s_{av}}/h}$. They only require that the ρ profile exhibit a local extremum (i.e. $\partial\rho/\partial y = 0$) at $y_{s_{av}}/h = 1$.

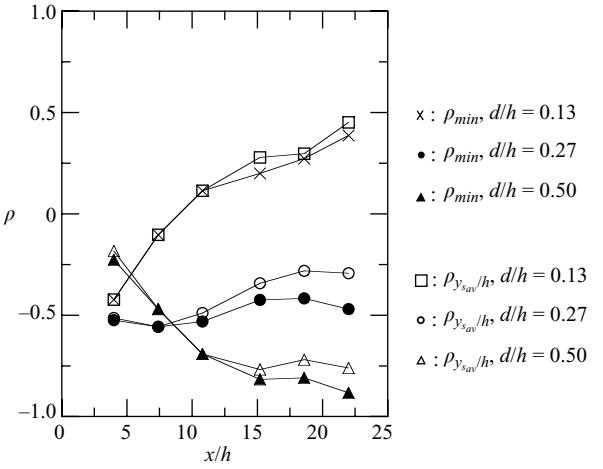

FIGURE 8. Comparison of ρ_{min} and $\rho_{y_{s_{av}}/h}$ for $y_{s_{av}}/h = 0.5$.

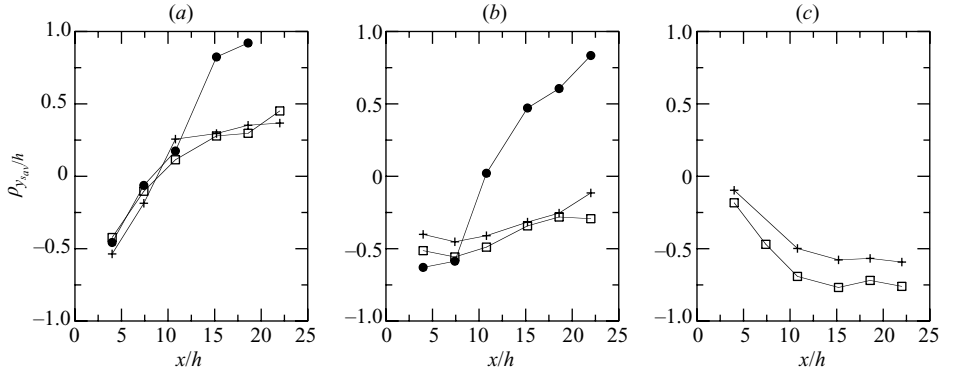

FIGURE 9. Evolution of $\rho_{y_{s_{av}}/h}$ with respect to the downstream position (x/h) for different average source positions $(y_{s_{av}}/h)$. (*a*) $d/h = 0.13$, (*b*) $d/h = 0.27$, (*c*) $d/h = 0.50$. ●, $y_{s_{av}}/h = 0.2$; □, $y_{s_{av}}/h = 0.5$; +, $y_{s_{av}}/h = 1.0$.

This extremum is, however, a minimum, as observed in the previous figure and the results of Warhaft (1984). However, in general, the two quantities differ, as can be seen in figure 8, which plots ρ_{min} and $\rho_{y_{s_{av}}/h}$ for $y_{s_{av}}/h = 0.5$. When $x/h \leqslant 10.8$, it is observed that ρ_{min} and $\rho_{y_{s_{av}}/h}$ are effectively equal. When $d/h = 0.27$ and 0.5, the differences in the two correlation coefficients are as high as $\Delta\rho = 0.2$. Nevertheless, given that the differences are not excessive, only $\rho_{y_{s_{av}}/h}$ is discussed herein in the interest of conciseness. A complete analysis of ρ_{min} can be found in Costa-Patry (2005).

Figure 9 shows the evolution of $\rho_{y_{s_{av}}/h}$ with respect to x/h for different $y_{s_{av}}/h$, holding d/h constant in each subfigure. Up to $x/h = 7.4$, the values of $\rho_{y_{s_{av}}/h}$ are similar for a given d/h. For $x/h > 7.4$, combinations with $y_{s_{av}}/h = 0.2$ rapidly increase towards $\rho_{y_{s_{av}}/h} = 1$. Such jumps were also seen by Tong & Warhaft (1995) in similar situations. For $x/h > 7.4$, the combinations with $y_{s_{av}}/h = 1.0$ generally exhibit larger $\rho_{y_{s_{av}}/h}$ than those with $y_{s_{av}}/h = 0.5$. Furthermore, note that the profiles with $d/h = 0.50$ start at $\rho_{y_{s_{av}}/h} = 0$ and continuously decrease; they are still in the first part of their development and the downstream domain is too short to observe their ultimate rise towards positive ρ.

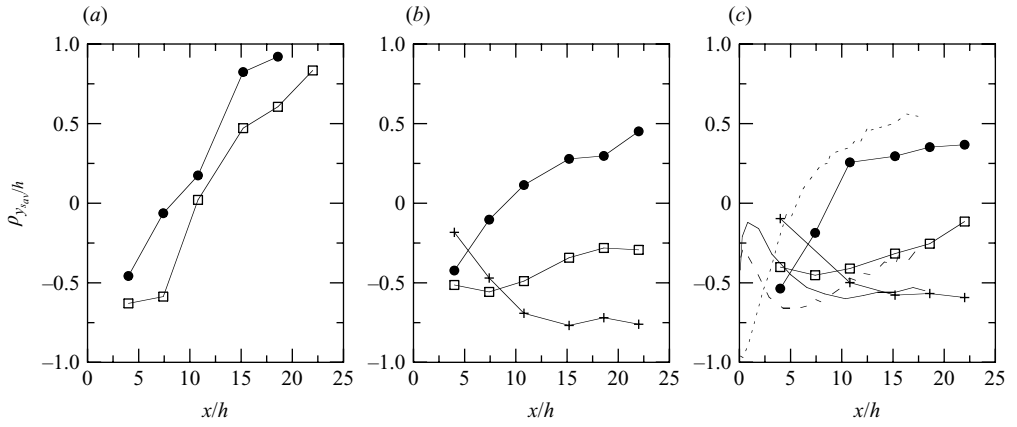

FIGURE 10. Evolution of $\rho_{y_{s_{av}}/h}$ with respect to the downstream position (x/h) for different source separations (d/h). (*a*) $y_{s_{av}}/h = 0.2$, (*b*) $y_{s_{av}}/h = 0.5$, (*c*) $y_{s_{av}}/h = 1.0$. ●, $d/h = 0.13$; □, $d/h = 0.27$; +, $d/h = 0.50$. The lines without data points in *c*) correspond to the data of Vrieling & Nieuwstadt (2003), figure 11. Short-dashed line: $d/h = 0.12$; long-dashed line: $d/h = 0.28$; solid line: $d/h = 0.4$.

Figure 10 plots the evolution of $\rho_{y_{s_{av}}/h}$ with respect to x/h for different d/h, holding $y_{s_{av}}/h$ constant in each subfigure. It is clear from these figures that the closer together the line sources (small d/h), the faster the correlation coefficient evolves from negative to positive values. Small d/h allows internal turbulent mixing to occur sooner as the thermal plumes will overlap more rapidly. Similarly to figure 9, figure 10 shows that, early downstream, d/h is a more important factor than $y_{s_{av}}/h$. In other words, early downstream, the mixing somewhat resembles that occurring in grid turbulence, where ρ is only a function of the separation distance between the line sources and the downstream position (Warhaft 1984). As expected, the effect of the inhomogeneity is largest when the sources are close to the wall.

In addition, the data of figure 10(*c*) can be directly compared with the results of the direct numerical simulation (DNS) of Vrieling & Nieuwstadt (2003), who calculated the thermal fields behind line sources located symmetrically about the channel centreline (i.e. for $y_{s_{av}}/h = 1.0$). The agreement between the present experiments and their DNS is good, and best for $x/h > 10$ when $d/h = 0.27$ and $d/h = 0.50$ (i.e. for the larger source separations). The fact that the agreement is best when d/h and x/h are large may imply that the effect of the initial conditions may be important when comparing experiments and DNS of dispersion from concentrated sources.

Figure 11 plots $\rho_{y_{s_{av}}/h}$ as a function of $y_{s_{av}}/h$. It is observed that the combinations with $y_{s_{av}}/h = 0.2$ separate from the others between $x/h \approx 10$ and 15. It appears that the high turbulence intensity at the wall rapidly increases $\rho_{y_{s_{av}}/h}$ for combinations with $y_{s_{av}}/h = 0.2$ through increased turbulent mixing. This does not affect other combinations with larger $y_{s_{av}}/h$ as they are too far from the wall.

Figure 12 plots $\rho_{y_{s_{av}}/h}$ as a function of d/h. As x/h increases, the results for the smallest separation ($d/h = 0.13$) increase more rapidly. The previously observed jump in $\rho_{y_{s_{av}}/h}$ for sources with $y_{s_{av}}/h = 0.2$ is also observed in these figures. Furthermore, the results for $y_{s_{av}}/h = 0.5$ and 1.0 behave in a similar manner; $\rho_{y_{s_{av}}/h}$ is generally higher with $y_{s_{av}}/h = 1.0$ than with $y_{s_{av}}/h = 0.5$. This is presumably due to the higher levels of mixing by wake flapping which are present for $y_{s_{av}}/h = 1.0$.

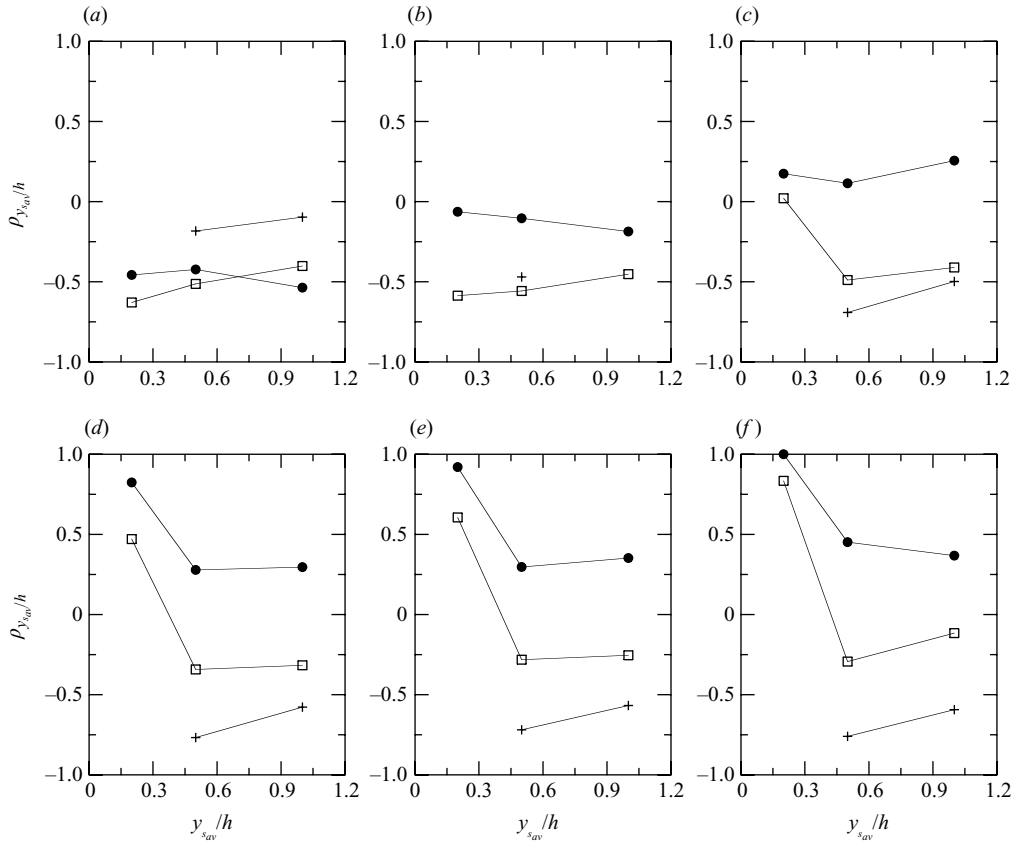

FIGURE 11. Evolution of $\rho_{y_{s_{av}}/h}$ with respect to the average position of the line sources ($y_{s_{av}}/h$) for different source separations (d/h). (*a*) $x/h = 4.0$, (*b*) $x/h = 7.4$, (*c*) $x/h = 10.8$, (*d*) $x/h = 15.2$, (*e*) $x/h = 18.6$, (*f*) $x/h = 22.0$. ●, $d/h = 0.13$; □, $d/h = 0.27$; +, $d/h = 0.50$.

4.2.3. *Comparisons with mixing in other flows*

As discussed in § 1, Warhaft (1984) was able to collapse the evolutions of ρ for the mixing of two scalars in isotropic turbulence. The correlation coefficient in isotropic turbulence was shown to be a function of two parameters, d/ℓ and $(x'/d)(v/U)$. Figure 9 showed the dominance of d/h in the mixing early downstream. Thus, some ρ evolution profiles appear similar to those in grid turbulence. However, it must be noted that this simplification only holds at best for $\rho_{y_{s_{av}}/h}$. The evolution of the ρ profiles presented in figure 7 is clearly dependent on d/h, $y_{s_{av}}/h$ and x/h at all times.

Figure 13 presents an attempt to collapse the $\rho_{y_{s_{av}}/h}$ evolutions with $y_{s_{av}}/h = 0.5$ and 1.0 using Warhaft's (1984) non-dimensionalization, $(x/d)(v/U)$, where v is the fluctuating RMS velocity in the wall-normal direction (evaluated at $y_{s_{av}}/h$), x/U represents the time from scalar insertion to probe measurement and d/v is the lateral convective time scale; v values were determined using the results of Moser, Kim & Mansour (1999). As is evident from figure 13, Warhaft's (1984) non-dimensionalization cannot account for the effect of the inhomogeneity – even for the two source locations least affected by the inhomogeneity: $y_{s_{av}}/h = 0.5$ and 1.0. Furthermore, it can be noted that the limited collapse of the data is worse for figure 13(*b*) than for figure 13(*a*). This is explained by the increased effect of the inhomogeneity for larger source separations

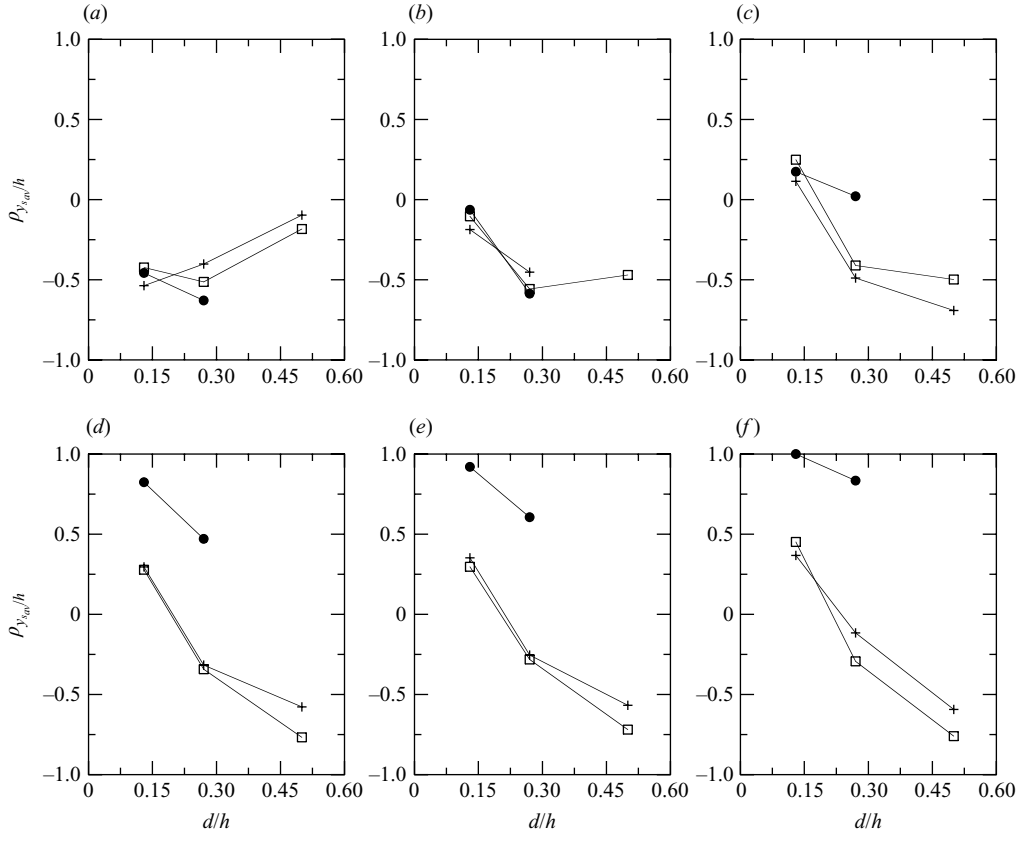

FIGURE 12. Evolution of $\rho_{y_{sqv}/h}$ with respect to the distance between line sources (d/h) for different average source positions $(y_{s_{av}}/h)$. (*a*) $x/h = 4.0$, (*b*) $x/h = 7.4$, (*c*) $x/h = 10.8$, (*d*) $x/h = 15.2$, (*e*) $x/h = 18.6$, (*f*) $x/h = 22.0$. ●, $y_{s_{av}}/h = 0.2$; □, $y_{s_{av}}/h = 0.5$; +, $y_{s_{av}}/h = 1.0$.

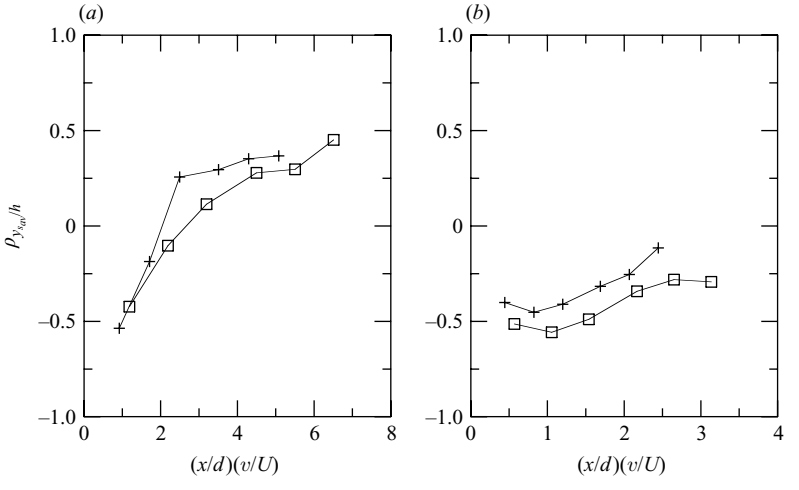

FIGURE 13. Non-dimensionalized downstream evolution of $\rho_{y_{sav}/h}$ for different average source positions $(y_{s_{av}}/h)$. (*a*) $d/h = 0.13$; (*b*) $d/h = 0.27$. □, $y_{s_{av}}/h = 0.5$; +, $y_{s_{av}}/h = 1.0$.

($d/h = 0.27$ in figure 13(*b*) versus $d/h = 0.13$ in figure 13(*a*)). Lastly, it is possible that a more complex non-dimensionalization could accurately collapse the present data; however, none was discovered.

Another possible parallel between grid turbulence and turbulent channel flow would be that, for combinations with $y_{s_{av}}/h = 1.0$, $\rho_{y_{s_{av}}/h}$ would share an equivalent evolution (up to a certain downstream distance) given that turbulent channel flow is almost homogeneous around $y/h = 1.0$. This assumption was used by Vrieling & Nieuwstadt (2003) to justify the comparison of their simulations with published experimental results (Warhaft 1984). To pursue this notion, it is worth comparing figure 14 of Warhaft (1984) and figure 9 of Tong & Warhaft (1995) with the results of figure 9. The former two figures plot the downstream evolution of $\rho_{y_{s_{av}}/h}$ in grid turbulence (Warhaft 1984) and in a turbulent jet (Tong & Warhaft 1995). A turbulent jet is both inhomogeneous and decaying, and is therefore more complex than grid turbulence (or turbulent channel flow, for that matter).

In view of figure 9, the results of Warhaft (1984), and those of Tong & Warhaft (1995), one can conclude that in turbulent channel flow, $\rho_{y_{s_{av}}/h}$ (with $y_{s_{av}}/h = 1.0$) evolves in a similar manner to $\rho_{y_{s_{av}}/h}$ in grid turbulence for the smaller downstream distances. Tong & Warhaft (1995) have shown that in a turbulent jet, ρ increases more rapidly than in grid turbulence. This was also observed for turbulent channel flow when $y_{s_{av}}/h = 0.2$, where the high turbulence intensity near the wall leads to faster mixing.

The mixing of thermal fields in such different flows can also be considered within the context of their structure. A principal difference between grid turbulence, turbulent jets, and turbulent channel flows is the bounded nature of the latter. The presence of the channel walls is clearly a significant factor and can have a variety of effects on the mixing therein.

First, the bounded nature of the flow limits the growth of the thermal plumes emanating from the concentrated sources. In other words, the plume width will never exceed the integral length scale of the flow. Whereas a scalar plume emitted from a concentrated source in homogeneous isotropic grid turbulence will exhibit three regimes in its evolution (molecular–diffusive, turbulent–convective, and turbulent–diffusive – Anand & Pope 1985; Stapountzis *et al.* 1986), a plume emitted in turbulent channel flow will never enter a turbulent–diffusive stage as it requires that the plume width be larger than the integral length scale of the turbulence†. Hence, similarly to unbounded flows, the growth of a plume within turbulent channel flow will be initially dominated by molecular diffusion, then by turbulent advection. However, far downstream, it will not grow due to the action of a traditional turbulent diffusivity, but rather will be subjected to shear flow dispersion (Taylor 1953, 1954). The latter is not applicable to the present work because it is valid only for very large downstream distances/times, well beyond the $x/h = 22.0$ limit of the current work. This limitation on the growth of a single plume must have a significant effect on the mixing of two scalars emitted from two sources.

It is difficult to quantitatively compare the results of Warhaft (1984) or those of Tong & Warhaft (1995) to ours for two reasons. First, given that both of the aforementioned flows are decaying, the properties of the flow change in the downstream direction (e.g. t_L, ℓ, the turbulence intensity, etc.). This is not the case in fully developed

† It should be pointed out that this limitation also holds for plume released from a concentrated source within a turbulent jet, given that the plume width cannot grow larger than the integral length scale/half-width of the jet.

turbulent channel flow. Secondly, the extent of the downstream measurements in Warhaft (1984) is quite different to those presented herein. For all but the smallest wire separation ($d = 1$ mm), Warhaft's (1984) measurements of ρ were distributed across the range $0.4 < t/t_L < 14$, so that he was also able to observe the mixing within the turbulent diffusive regime, which occurs for $t \gg t_L$. The present measurements spanned the range $0.4 < t/t_L < 2.0$ (based on $t = x/\langle U \rangle_{y/h=1}$), leaving generally two data points of Warhaft (1984) with which to compare. (The range of t/t_L in the experiments of Tong & Warhaft (1995) extends from 0.1 to 1.6.)

Nevertheless, we can attempt to explain the above-mentioned qualitative observation that the near-wall mixing of two scalars fields in a bounded flow may be better than that in homogeneous isotropic turbulence. First, the channel walls limit the spread of the plumes, allowing the plume from the source located farther from the wall to 'catch up' and mix with the other plume emitted from the source closest to the wall. In an unbounded flow, it is conceivable that the edges of the plume will be composed solely of scalar that was emitted from the source closest to that side of the plume. Consequently, the mixing at the edges of the plume may be better in a bounded flow. Furthermore, the turbulent kinetic energy is highest near the walls in a turbulent channel flow, thus further increasing the near-wall mixing that occurs in a plume that approaches one or both walls. Such a notion is consistent with PDFs of the scalar field behind single line sources in turbulent channel flow (Lavertu & Mydlarski 2005). In that work, it was observed that near-wall PDFs exhibited better mixing (by being much more Gaussian in shape) that those farther from the wall (which were more exponential in nature). Lavertu & Mydlarski (2005) associated the exponential PDFs of the scalar field with flapping of the plume. For near-wall sources, such PDFs were only observed near the edges of the plume. However, the PDFs for plumes released at the channel centreline were exponential in nature for all transverse locations (i.e. even directly behind the source) and for all but the farthest downstream distances. This was associated with more intense flapping of the plume for centreline sources, given that there is no nearby wall to limit the flapping. Because the flapping of plumes is a large-scale coherent motion, it does not serve to mix two plumes well, which is consistent with the observed anticorrelation of the two scalar fields. Lastly, when the plume has spread all the way to a wall, entrainment of ambient 'scalar-free' fluid will no longer be possible from that side of the plume, thus enhancing the mixing.

In summary, the presence of the wall in channel flow serves to improve the mixing by three mechanisms: (i) limiting the growth of the plume, (ii) increasing the turbulent mixing due to the increased turbulent kinetic energy near the wall, and (iii) limiting the flapping of the plume, which inhibits mixing (since both plumes are advected together and do not interact) and leads to anticorrelation of the scalar fluctuations. None of these factors play a role in grid turbulence where the plume growth is unlimited, the turbulent kinetic energy is constant given the flow's homogeneity, and there is nothing limiting the flapping of the plume by the largest eddies (until, of course, the plume grows to be larger than these eddies). In a turbulent jet, the integral length scale of a thermal field rapidly grows to the same order as that of the velocity field, then continues to grow at the same rate as the velocity field (Tong & Warhaft 1995). Therefore, the scalar field is, in a sense, bounded by the extent of the turbulent jet, even though it can nevertheless continue to grow and entrain ambient fluid. Furthermore, in a jet, the turbulent kinetic energy is largest in the core of the jet, not at its boundaries, unlike turbulent channel flow.

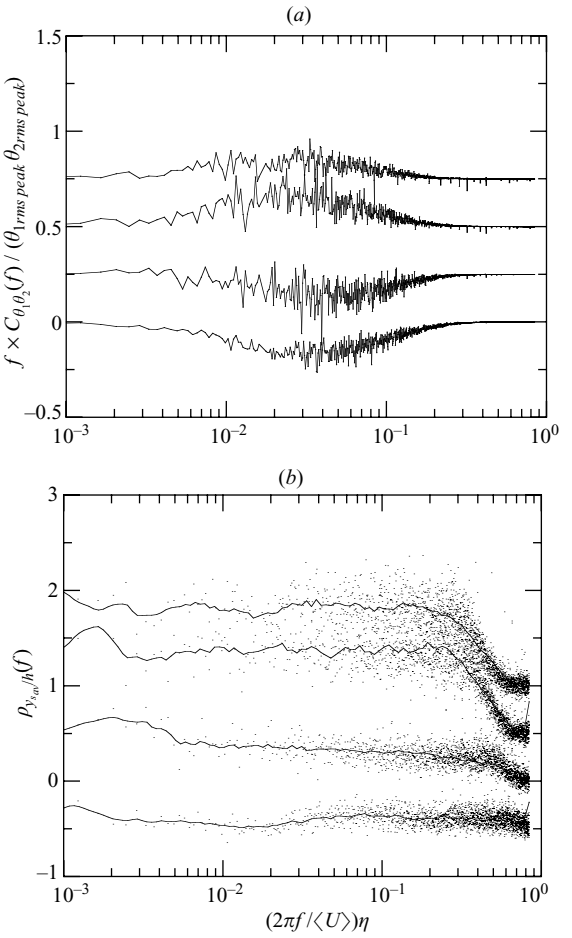

FIGURE 14. Cospectra and coherency spectra for case B ($y_{s_{av}}/h = 0.5$, $d/h = 0.13$) measured at $y = y_{s_{av}}/h$. (*a*) Cospectra. From bottom to top, the curves correspond to $x/h = 4.0$, $x/h = 7.4$, $x/h = 15.2$ and $x/h = 18.6$. Each subsequent curve has been shifted up by 0.25 with respect to the previous curve. (*b*) Coherency spectra. From bottom to top, the curves correspond to $x/h = 4.0$, $x/h = 7.4$, $x/h = 15.2$ and $x/h = 18.6$. Each subsequent curve has been shifted up by 0.50 with respect to the previous curve. Note that the curves are fits (Stineman 1980) to the coherency data, shown as dots. (Given that the coherency is defined as a ratio of spectra, the coherency spectra are noisier than the individual spectra or cospectra.)

4.3. *Scalar cospectra and coherency spectra*

In this section, a representative selection of the nine line source combinations (cases B, D and I) is studied by means of spectral analysis to investigate the mixing at different scales. Figures 14–16 show the cospectra, $C_{\theta_1\theta_2}(f)$, and coherency spectra, $\rho(f)$ ($\equiv C_{\theta_1\theta_2}(f)/[E_{\theta_1}(f)E_{\theta_2}(f)]^{1/2}$), for these source combinations. Consistent with the approach of Tong & Warhaft (1995), the cospectra are non-dimensionalized by dividing by the peak of the θ_{rms} profiles behind single line sources and multiplying by frequency. Plotted in this manner, the area under the cospectra is then proportional to the covariance.

It can be concluded from figures 14(*a*), 15(*a*) and 16(*a*) that most of the production of covariance (negative or positive) is contained between $\kappa\eta = 0.01$ and 0.1 (10 to

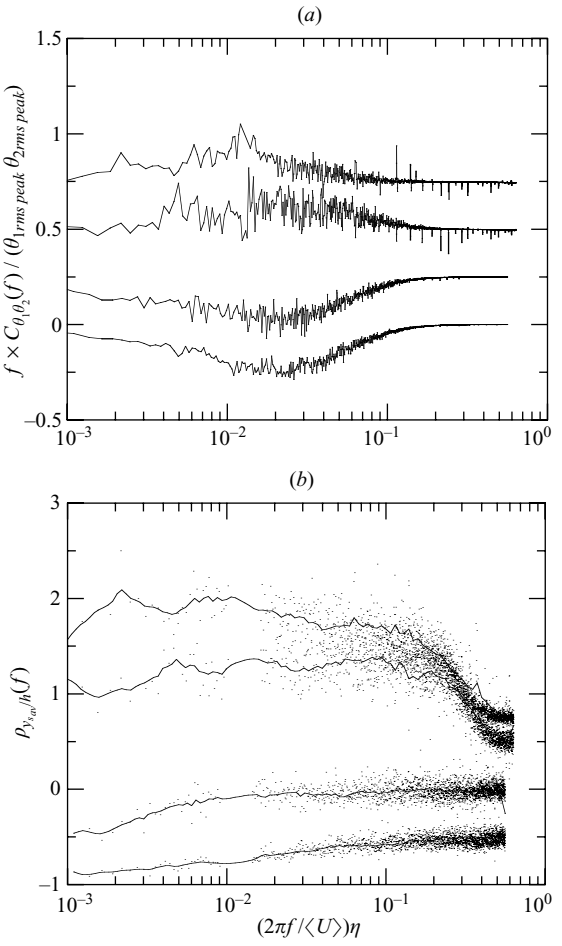

FIGURE 15. As figure 14 but for case D ($y_{s_{av}}/h = 0.2$, $d/h = 0.27$).

100 times the Kolmogorov microscale (the integral scale is approximately 100η in the present flow), where $2\pi f/\langle U\rangle$ is the wavenumber, κ. As would be expected, the downstream evolution of the cospectra follows the downstream evolution of the correlation coefficient. In other words, negative cospectra occur when ρ is negative, etc. The general trend towards positive covariance as x/h increases is clear from the figures. Furthermore, it also appears that the peak in the covariance occurs for lower frequencies (i.e. larger scales) with increasing x/h. This is most evident in figures 14(a) and 15(a), which plot data for the largest 'effective' downstream distances because the data presented therein is for the smallest wire separations ($d/h = 0.13$ and 0.27, respectively).

The coherency spectrum (i.e. the non-dimensionalized cospectrum) can be considered as a spectral correlation coefficient. For the smallest x/h, it can be observed that the coherency spectrum at large scales (i.e. lower frequencies) is more negative than that at small scales. This derives from the initial anti-correlation associated with simultaneous flapping of both plumes by large-scale eddies. Furthermore, the downstream distance to which this observation continues to hold increases with increasing wire separation (d/h). This is attributed to the previously mentioned inverse relationship between the interaction of the two scalar fields and the source

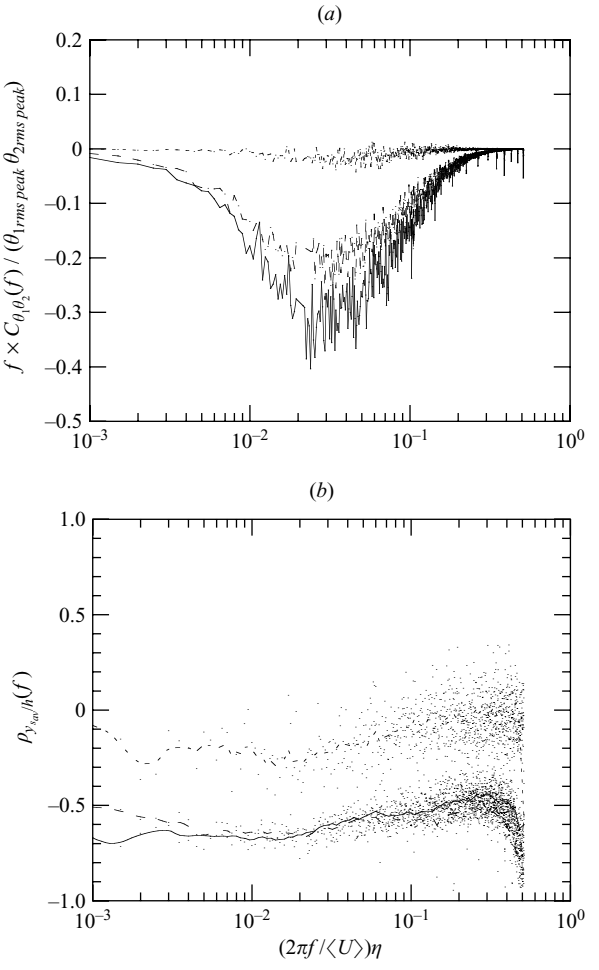

FIGURE 16. Cospectra and coherency spectra for case I ($y_{s_{av}}/h = 1.0$, $d/h = 0.5$) measured at $y = y_{s_{av}}/h$. $x/h = 4.0$: dotted line; $x/h = 7.4$: solid line; $x/h = 15.2$: dashed line. (*a*) Cospectra. (*b*) Coherency spectra.

separation. (Clearly, plumes emitted from sources with large separations will take longer to interact than ones emitted from sources with small separations. Recall that $(x'/d)(v/U)$ was found to collapse the data well in homogeneous turbulence (Warhaft 1984), though this normalization is less successful in collapsing the present data.) For these coherency spectra, the small scales are closer to zero, given that the scalar fields in this region have not yet experienced much internal turbulent mixing. However, they are clearly negative, as was also observed in Tong & Warhaft (1995).

For locations farther downstream, the coherency spectra develop a quasi-plateau over all but the smallest scales. Its value corresponds to the overall correlation coefficient for the same conditions (i.e. same $y_{s_{av}}/h$, d/h, x/h, and y/h) and therefore tends to positive values for larger x/h. The value of the coherency at small scales seems to lag behind the large-scale coherency in its evolution. This could be due to the additional time required for the coherence to be transferred to smaller scales. If so, the small-scale coherency should eventually asymptote to the values observed at large scales, as was observed in the turbulent jet of Tong & Warhaft (1995). That

being said, the large-scale coherency observed herein is smaller than that observed in Tong & Warhaft (1995) for their farthest downstream distance (even though both sets of experiments span similar ranges of t/t_L). The difference may be related to the entrainment of ambient air in the turbulent jet, because, as explained by Tong & Warhaft (1995), 'the entrainment of the ambient air by the jet starts to produce similar structures in both scalar fields, and thus $\rho(f)$ tends towards positive values at large scales'. Though there is clearly no entrainment of ambient fluid in the present turbulent channel flow, the relationship between the large-scale mixing of the plume (with the surrounding fluid) and the the large-scale coherency has yet to be determined.

Finally, it is of interest to point out that near the wall (figure 15, case D), the high turbulence intensity results in a noticeable variation in the coherency across the scales. The large-scale coherency changes much faster than that of the small scales. Furthermore, it is for this case that the coherency spans the largest range of values ($-0.8 \leqslant \rho(f) \leqslant 0.5$). Given that turbulence production is a large-scale phenomenon, its effect is probably first felt at low frequencies and, as mentioned above, will only be felt at the smaller scales after sufficient time has passed for the mixing to be transferred down to the smaller scales. Of the three coherency spectra presented herein, that for figure 15 (case D) most closely resembled the results of Tong & Warhaft (1995), which were only given for one pair of source locations. (Had they presented coherency spectra for other source combinations, they would have undoubtedly also observed different evolutions of $\rho(f)$. This, however, was not the main focus of their study.)

5. Conclusions

The objective of this work was to study the mixing of two scalars in turbulent channel flow and, more specifically, to analyse the evolution and interaction of two thermal fields released from concentrated sources. To this end, nine combinations of source locations were studied at six different downstream distances for a total of 54 sets of measurements. Transverse profiles of (i) the mean excess temperature, (ii) the RMS temperature fluctuations, and (iii) the correlation coefficient were studied. Typical cospectra and coherency spectra of the two temperature fields were also presented.

It was shown that the mean temperature excess profiles could be deduced from those emitted from a single source. However, the additive property of the mean temperature excess profiles emitted from two line sources was not exhibited by the corresponding θ_{rms} profiles, which were therefore studied in detail. They were found to depend on three parameters: (i) the separation distance between the line sources (d/h), (ii) their average wall-normal position ($y_{s_{av}}/h$), and (iii) the downstream position (x/h) of the measurement probe.

The transverse θ_{rms} profiles produced by two sources revealed some similarities with those emitted from one source. For example, the peak of the θ_{rms} profiles drifted towards $y/h = 1.0$ for line source pairs with $y_{s_{av}}/h = 0.2$ and 0.5. Furthermore, the peak of the θ_{rms} profiles emitted from two sources decayed with increasing downstream distance. Many differences also existed. Some of the transverse profiles exhibited double peaks in the early stages of their evolution. Double peaks were the most persistent for source locations with $y_{s_{av}}/h = 1.0$ (where flapping of the thermal wakes was strongest and internal turbulent mixing the weakest). They were the least common for sources with $y_{s_{av}}/h = 0.2$ (where flapping of the wakes was the weakest and turbulent mixing the strongest). In addition, the downstream decay of the peaks of the measured θ_{rms} profiles was not well represented by a power law

(excluding situations where the two wakes had not yet interacted), unlike θ_{rms} profiles generated by one source.

The correlation coefficient (ρ) was used to evaluate the mixing of the two scalars. It was also found to depend on d/h, $y_{s_{av}}/h$, x/h, and y/h. When measured within regions that are exposed to the instantaneous plumes of each line source, the correlation coefficient is no longer undefined and initially takes on small negative values. Farther downstream, the correlation coefficient becomes increasingly negative, due to the early dominance of flapping of the thermal wakes by turbulent eddies (before the wakes have widened significantly). The correlation coefficients' subsequent increase and tendency towards positive correlations, and perhaps ultimately an asymptotic value, were not observed for most cases, given the finite length of the channel test section. Usually, ρ was highest in the tails of the profiles, where θ_{rms} was small. This was attributed to strong, but rare, eddies that would advect (in the transverse direction) both thermal wakes far away from their sources. Minima in ρ were observed for transverse locations near $y_{s_{av}}/h$ when wake flapping was prominent (i.e. for $y_{s_{av}}/h = 0.5$ and 1.0). The minima in ρ drifted towards the wall as x/h increased for $y_{s_{av}}/h = 0.2$ and 0.5.

To facilitate the comparison of the correlation coefficient resulting from different combinations of source locations, $\rho_{y_{s_{av}}/h}$ was studied. The separation distance between the two line sources was a dominant factor in its evolution; the closer the line sources were, the faster their thermal fields mixed. The effect of $y_{s_{av}}/h$ was less significant – especially for small x/h – except when near the wall. Here, the high level of turbulence was found to accelerate the mixing, causing the correlation coefficient to increase rapidly.

For source pairs with $y_{s_{av}}/h = 1.0$ (i.e. sources located in the least inhomogeneous region of the flow), $\rho_{y_{s_{av}}/h}$ evolved in a similar manner to that observed in homogeneous isotropic grid-generated turbulence. Nevertheless, attempts to reduce the number of relevant parameters for $\rho_{y_{s_{av}}/h}$, as done in grid turbulence (Warhaft 1984), were unsuccessful, thus demonstrating the non-negligible effect of the inhomogeneity of channel flow.

The cospectra followed the same trends as ρ, decreasing then increasing with downstream distance. The coherency spectra exhibited large scales that evolved more rapidly than the small scales. In addition, the fast evolution of the large scales was most evident when the sources were located close to the wall, where the turbulence intensity, and therefore mixing, was the most vigourous.

The authors would like to thank Georges Tewfik and Thomas Lavertu for their help. Support was provided by the Natural Sciences and Engineering Research Council of Canada and the Fonds québécois de la recherche sur la nature et les technologies. Some preliminary experiments were performed by Elise Delepouve. Finally, the authors thank the reviewers for their constructive comments.

REFERENCES

Anand, M. S. & Pope, S. B. 1985 Diffusion behind a line source in grid turbulence. In *Proc. 4th Symp. on Turbulent Shear Flows, Karlsruhe, Germany*, pp. 46–61. Springer.

Beaulac, S. & Mydlarski, L. 2004 Dependence on the initial conditions of scalar mixing in the turbulent wake of a circular cylinder. *Phys. Fluids* **16**, 3161–3172.

Bernard, P. S. & Rovelstad, A. L. 1994 On the physical accuracy of scalar transport modelling in inhomogeneous turbulence. *Phys. Fluids* **6**, 3093–3108.

Brethouwer, G. Boersma, B. J., Pourquié, M. B. J. M. & Nieuwstadt, F. T. M. 1999 Direct numerical simulation of turbulent mixing of a passive scalar in pipe flow. *Eur. J. Mech.* B/*Fluids* **18**, 739–756.

Browne, L. W. B. & Antonia, R. A. 1987 The effect of wire length on temperature statistics in a turbulent wake. *Exps. Fluids* **5**, 426–428.

Costa-Patry, E. 2005 Mixing of two scalars in turbulent channel flow. M. Eng. Thesis, McGill University.

Durbin, P. A. 1982 Analysis of the decay of temperature fluctuations in isotropic turbulence. *Phys. Fluids* **25**, 1328–1332.

El Kabiri, M., Paranthoen, P., Rosset, L. & Lecordier, J. C. 1998 Fluctuations de temperature et flux de chaleur en aval d'une source linéaire placée dans une couche limite turbulente. *Rev. Gén. Therm.* **37**, 181–194.

Grandmaison, E. W., Pollard, A. & Ng, S. 1991 Scalar mixing in a free, turbulent rectangular jet. *Intl J. Heat Mass Transfer* **34**, 2653–2662.

Ilipoulos, I., & Hanratty, T. J. 1999 Turbulent dispersion in a non-homogenous field. *J. Fluid Mech.* **392**, 45–71.

Incropera, F. P., Kerby, J. S., Moffatt, D. F. & Ramadhyani, S. 1986 Convection heat transfer from discrete heat sources in a rectangular channel. *Intl J. Heat Mass Transfer* **29**, 1051–1058.

Karnik, U. & Tavoularis, S. 1989 Measurements of heat diffusion from a continuous line source in a uniformly sheared turbulent flow. *J. Fluid Mech.* **202**, 233–261.

Kim, J., Moin, P. & Moser, R. 1987 Turbulence statistics in fully developed channel flow at low Reynolds number *J. Fluid Mech.* **177**, 133–166.

Kontomaris, K. & Hanratty, T. J. 1994 Effect of a molecular diffusivity on point source diffusion in the centre of a numerically simulated turbulent channel flow. *Intl J. Heat Mass Transfer* **37**, 1817–1828.

Kraichnan, R. H. 1968 Small-scale structure of the scalar field convected by turbulence. *Phys. Fluids* **11**, 945–953.

Kraichnan, R. H. 1974 Convection of a passive scalar by a quasi-uniform random straining field. *J. Fluid Mech.* **64**, 737–762.

Kraichnan, R. H. 1994 Anomalous scaling of a randomly advected passive scalar. *Phys. Rev. Lett.* **72**, 1016–1019.

LaRue, J. C., Deaton, T. & Gibson, C. H. 1975 Measurement of high-frequency turbulent temperature. *Rev. Sci. Instrum.* **46**, 757–764.

Lavertu, R. A. 2002. Scalar dispersion in turbulent channel flow. M.Eng. Thesis, McGill University.

Lavertu, R. A. & Mydlarski, L. 2005 Scalar mixing from a concentrated source in turbulent channel flow. *J. Fluid Mech.* **528**, 135–172.

Lemay, J. & Jean, Y. 2001 *Constant Current Anemometer Utilization Guide*. University Laval, Quebec, Canada.

Lemay, J. & Benaïssa, A. 2001 Improvement of cold-wire response for measurement of temperature dissipation, *Exps. Fluids* **31**, 347–356.

Lyons, S. L. & Hanratty, T. J. 1991 Direct numerical simulation of passive heat transfer in a turbulent channel flow. *Intl J. Heat Mass Transfer* **34**, 1149–1161.

Moser, R. D., Kim, J. & Mansour, N. N. 1999 Direct numerical simulation of turbulent channel flow up to $Re_\tau = 590$. *Phys. Fluids* **11**, 943–945.

Mydlarski, L. & Warhaft, Z. 1998 Passive scalar statistics in high-Péclet-number grid turbulence. *J. Fluid Mech.* **358**, 135–175.

Na, Y. & Hanratty, T. J. 2000 Limiting behaviour of turbulent scalar transport close to a wall. *Intl J. Heat Mass Transfer* **43**, 1749–1758.

Orlandi, P. & Leonardi, S. 2004 Passive scalar in a turbulent channel flow with wall velocity disturbances. *Flow, Turb. Combust.* **72**, 181–197.

Papavassiliou, D. V. & Hanratty, T. J. 1997 Transport of a passive scalar in a turbulent channel flow. *Intl J. Heat Mass Transfer* **40**, 1303–1311.

Paranthoen, P., Fouari, A., Dupont, A., & Lecordier, J. C. 1988 Dispersion measurements in turbulent flows (boundary layer and plane jet). *Intl J. Heat Mass Transfer* **31**, 153–165.

Pope, S. B. 2000 *Turbulent Flows*. Cambridge University Press.

Poreh, M. & Cermak, J. E. 1964 Study of diffusion from a line source in a turbulent boundary layer. *Intl J. Heat Mass Transfer* **7**, 1083–1095.

Poreh, M. & Hsu, K. S. 1971 Diffusion from a line source in a turbulent boundary layer. *Intl J. Heat Mass Transfer* **14**, 1473–1483.

Shah, D. A., Chambers, A. J. & Antonia, R. A. 1983 Reynolds number dependence of a fully developed turbulent duct flow. *Eighth Australian Fluid Mechanics Conference, University of New Castle.*

Shlien, D. J. & Corrsin, S. 1976 Dispersion measurements in a turbulent boundary layer. *Intl J. Heat Mass Transfer* **19**, 285–295.

Shraiman, B. I. & Siggia, E. D. 2000 Scalar turbulence. *Nature* **405**, 639–646

Sreenivasan, K. R. 1991 On local isotropy of passive scalars in turbulent shear flows. *Proc. R. Soc. Lond.* A **434**, 165–182.

Sreenivasan, K. R., Tavoularis, S., Henry, R. & Corrsin, S. 1980 Temperature fluctuations and scales in grid-generated turbulence, *J. Fluid Mech.* **100**, 597– 621.

Stapountzis, H., Sawford, B. L., Hunt, J. C. R. & Britter, R. E. 1986 Structure of the temperature field downwind of a line source in grid turbulence. *J. Fluid Mech.* **165**, 401–424.

Stineman, R. W. 1980 A consistently well-behaved method of interpolation. *Creative Comput.* **7**, 54–57.

Taylor, G. I. 1935. Statistical theory of turbulence. IV-Diffusion in a turbulent air stream. *Proc. R. Soc. Lond.* A **151**, 465–478.

Taylor, G. I. 1953 Dispersion of soluble matter in solvent flowing slowly through a tube. *Proc. R. Soc. Lond.* A **219**, 186–203.

Taylor, G. I. 1954 The dispersion of matter in turbulent flow through a pipe. *Proc. R. Soc. Lond.* A **223**, 446–468.

Tong, C. & Warhaft, Z. 1995 Passive scalar dispersion and mixing in a turbulent jet. *J. Fluid Mech.* **292**, 1–38.

Townsend, A. A. 1954 The diffusion behind a line source in homogeneous turbulence. *Proc. R. Soc. Lond.* A **224**, 487.

Uberoi, M. S. & Corrsin, S. 1953 Diffusion from a line source in isotropic turbulence. *NACA Tech. Note* 2710 (also *NACA Rep.* 1142).

Veeravalli, S. & Warhaft, Z. 1990 Thermal dispersion from a line source in the shearless turbulence mixing layer. *J. Fluid Mech.* **216**, 35–70.

Villermaux E., Innocenti, C. & Duplat, J. 2001 Short circuits in the Corrsin-Obukhov cascade. *Phys. Fluids* **13**, 284–289.

Vinçont, J. Y., Simoens, S., Ayrault, M. & Wallace, J. M. 2000 Passive scalar dispersion in a turbulent boundary layer from a line source at the wall and downstream of an obstacle. *J. Fluid Mech.* **424**, 127–167.

Vrieling, A. J. & Nieuwstadt, F. T. M. 2003 Turbulent dispersion from nearby point sources–interference of the concentration statistics. *Atmos. Env.* **37**, 4493–4506.

Warhaft, Z. 1981 The use of dual heat injection to infer scalar covariance decay in grid turbulence. *J. Fluid Mech.* **104**, 93–109.

Warhaft, Z. 1984 The interference of thermal fields from line sources in grid turbulence. *J. Fluid Mech.* **144**, 363–387.

Warhaft, Z. 2000 Passive scalars in turbulent flows. *Annu. Rev. Fluid Mech.* **32**, 203–240.

Warhaft, Z. & Lumley, J. L. 1978 An experimental study of the decay of temperature fluctuations in grid-generated turbulence, *J. Fluid Mech.* **188**, 659–684.

Wyngaard, J. C. 1971 Spatial resolution of a resistance wire temperature sensor. *Phys. Fluids* **14**, 2052–2054.